



Exponential suppression of bit-flips in a qubit encoded in an oscillator

Raphaël Lescanne^{1,2}, Marius Villiers^{1,2}, Théau Peronnin³, Alain Sarlette², Matthieu Delbecq¹, Benjamin Huard ³, Takis Kontos¹, Mazyar Mirrahimi² and Zaki Leghtas ^{1,2,4}✉

A quantum system interacts with its environment—if ever so slightly—no matter how much care is put into isolating it¹. Therefore, quantum bits undergo errors, putting dauntingly difficult constraints on the hardware suitable for quantum computation². New strategies are emerging to circumvent this problem by encoding a quantum bit non-locally across the phase space of a physical system. Because most sources of decoherence result from local fluctuations, the foundational promise is to exponentially suppress errors by increasing a measure of this non-locality^{3,4}. Prominent examples are topological quantum bits, which delocalize information over real space and where spatial extent measures non-locality. Here, we encode a quantum bit in the field quadrature space of a superconducting resonator endowed with a special mechanism that dissipates photons in pairs^{5,6}. This process pins down two computational states to separate locations in phase space. By increasing this separation, we measure an exponential decrease of the bit-flip rate while only linearly increasing the phase-flip rate⁷. Because bit-flips are autonomously corrected, only phase-flips remain to be corrected via a one-dimensional quantum error correction code. This exponential scaling demonstrates that resonators with nonlinear dissipation are promising building blocks for quantum computation with drastically reduced hardware overhead⁸.

Protecting quantum states against decoherence is a fundamental problem in physics, and is pivotal for the future of quantum computing. The theory of quantum error correction (QEC)^{9,10} and its fault-tolerant implementation provides a solution. In QEC, groups of noisy physical quantum bits (qubits) are arranged together to encode qubits with reduced noise, and fault tolerance establishes that noisy quantum computers can operate reliably if the noise is below a threshold. A strong focus in quantum architecture design has been to increase this threshold to a value within experimental reach, but the required hardware overhead remains daunting². Therefore, there is a pressing need for new ideas to encode and protect quantum information.

Let us start by understanding why classical information is so stable. Consider a light switch that has two stable states labelled 0 and 1. Their stability is provided by two properties. First, to change states one needs to apply a force to overcome an energy barrier, usually provided by the deformation of a spring. Second, friction between mechanical parts is essential for stability: when a perturbation randomly deviates the switch from its stable state, the gained entropy must be dissipated into a reservoir in order to recover the initial state. Can these two properties be transposed to protect quantum information?

The $|0\rangle$ and $|1\rangle$ states of a qubit, such as the electronic orbitals of an ion or energy levels of a nonlinear resonator, often have overlapping supports in phase space. First, one needs to isolate the two states so that they no longer overlap^{11,12} and separate them by an energy barrier^{13–18}. The second property, friction (or dissipation), leaks information about the system and therefore seems incompatible with the requirement for a qubit to adopt quantum superpositions of states. Remarkably, there exists a dissipative mechanism, known as two-photon dissipation, which stabilizes the $|0\rangle$ and $|1\rangle$ states of a qubit without affecting quantum superpositions of the two⁵.

Recent superconducting circuit experiments^{6,19} have demonstrated that a resonator endowed with two-photon dissipation develops a manifold of steady states spanned by two states, $|0\rangle_\alpha$ and $|1\rangle_\alpha$, lying in two distinct locations of the resonator two-dimensional (2D) phase space. The combination of dissipation and non-locality should prevent random swaps between $|0\rangle_\alpha$ and $|1\rangle_\alpha$ (bit-flips). However, circuit architectures mediating two-photon dissipation impinged errors on the resonator. These experiments fell short of crossing the demanding threshold where the correction is faster than the occurrence of all errors, including those induced by the correcting mechanism itself.

In this work, we measure an exponential decrease of the bit-flip rate as we increase the separation between states $|0\rangle_\alpha$ and $|1\rangle_\alpha$, while only linearly increasing the phase-flip rate (errors that scramble the phase of a superposition of $|0\rangle_\alpha$ and $|1\rangle_\alpha$). The bit-flip time reaches 1 ms, a 300-fold improvement over the energy decay time of the resonator. This was made possible by inventing a circuit that mediates a pristine nonlinear coupling between the resonator and its environment, thus circumventing the problems of previous implementations^{6,19}. Our qubit combines two unique features: only phase-flips remain to be actively corrected^{8,20–22} and its 2D phase space can be accessed to perform gates^{7,8,23,24}, making it an ideal building block for scalable fault-tolerant quantum computation with a significant reduction in hardware overhead⁸.

We follow the paradigm of cat-qubits^{7,25}, where information is encoded in quantum superpositions of resonator states (Fig. 1):

$$\begin{aligned}|0\rangle_\alpha &= \frac{1}{\sqrt{2}}(|+\rangle_\alpha + |-\rangle_\alpha) = |+\alpha\rangle + \mathcal{O}(e^{-2|\alpha|^2}) \\|1\rangle_\alpha &= \frac{1}{\sqrt{2}}(|+\rangle_\alpha - |-\rangle_\alpha) = |-\alpha\rangle + \mathcal{O}(e^{-2|\alpha|^2})\end{aligned}$$

where $|\pm\rangle_\alpha = \mathcal{N}_\pm(|\alpha\rangle \pm |-\alpha\rangle)$, $|\alpha\rangle$ is a coherent state with complex amplitude α and $\mathcal{N}_\pm = 1/\sqrt{2(1 \pm e^{-2|\alpha|^2})}$. All these states contain an average number of photons of $\sim |\alpha|^2$ for $|\alpha| > 1$. A significant

¹Laboratoire de Physique de l'Ecole Normale Supérieure, ENS, Université PSL, CNRS, Sorbonne Université, Université de Paris, Paris, France. ²QUANTIC team, INRIA de Paris, Paris, France. ³Université Lyon, ENS de Lyon, Université Claude Bernard Lyon 1, CNRS, Laboratoire de Physique, Lyon, France. ⁴Centre Automatique et Systèmes, Mines-ParisTech, PSL Research University, Paris, France. ✉e-mail: zaki.leghtas@mines-paristech.fr

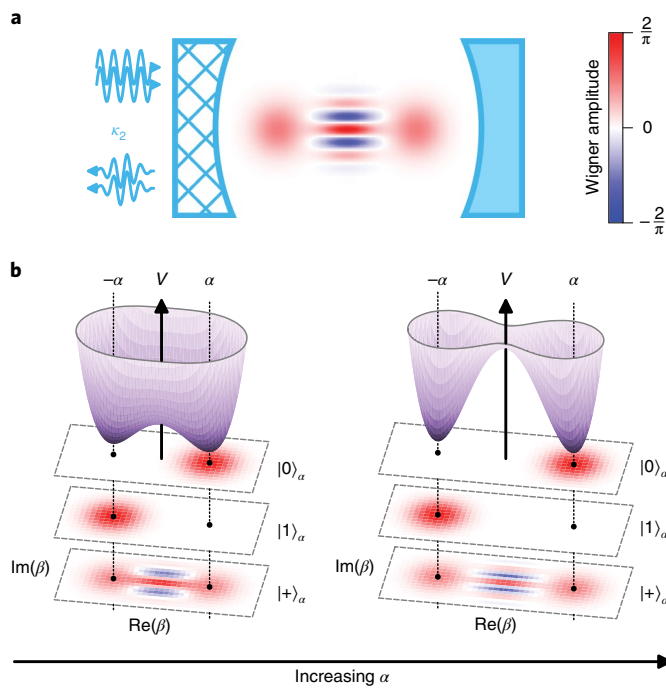


Fig. 1 | The cat-qubit. **a**, Quantum information is encoded in a resonator (blue mirrors) coupled to its environment through a special apparatus (hatched mirror) where pairs of photons are exchanged at rate κ_2 (double arrows). **b**, The dynamics are illustrated by a pseudo-potential V (purple) defined over the resonator quadrature phase space (β plane). The cat-qubit states $|0\rangle_a$ and $|1\rangle_a$ lie in the minima of V and are separated in phase space as shown by their Wigner representations (stacked colour plots). Bit-flip errors, which randomly swap $|0\rangle_a$ and $|1\rangle_a$, are exponentially suppressed by increasing this separation. Crucially, this pseudo-potential does not alter quantum superpositions of $|0\rangle_a$ and $|1\rangle_a$, such as the Schrödinger cat state $|+\rangle_a$.

source of errors in a resonator is energy decay, which collapses all states ($|0\rangle_a$ and $|1\rangle_a$ included) towards the vacuum, thus erasing any encoded information. This decay is balanced by a mechanism where the resonator exchanges only pairs of photons with its environment⁵ (Fig. 1a), known as two-photon dissipation. This dynamics is modelled by the following loss operator

$$L_2 = \sqrt{\kappa_2}(a^2 - a^{\dagger 2}) \quad (1)$$

where a is the annihilation operator of the resonator, κ_2 is the rate at which pairs of photons are exchanged with the environment and the term in a^2 results from a drive that inserts pairs of photons (see Supplementary Information). The cat-qubit states $|0\rangle_a$, $|1\rangle_a$ and all their superpositions are steady states of this dynamics. A convenient tool to visualize the semiclassical dynamics of equation (1) is the pseudo-potential V defined over the complex plane as $-\nabla V(\beta) = \frac{d\phi}{dt}$, where β is the expectation value of a at time t in a semiclassical approximation (see Supplementary Information). Stable steady states are local minima of V (Fig. 1b) and correspond to $\beta = \pm\alpha$. An error process can disrupt the stability of these states and induce transitions between them. By analogy with a particle in a double well potential, tunnelling (or bit-flips) from one well to another is exponentially suppressed in the separation between the two wells (here defined as $|\alpha|^2$), as long as the error process fulfils two criteria: it has to be local and sufficiently weak. An error process is local if it transforms a state into neighbouring states in phase space²⁶. As an example, dominant errors such as photon loss, gain

and dephasing are local. Moreover, the effective error rate κ_{err} must be weaker than the confining rate $\kappa_{\text{conf}} = 2|\alpha|^2\kappa_2$ (see Supplementary Information) inherited from the confining potential V , in order for the cat-qubit states to remain localized near the potential minima. The outstanding challenge to observe an exponential increase in the bit-flip time is therefore to engineer $\kappa_{\text{conf}} > \kappa_{\text{err}}$ for all dominant local error processes.

Two-photon exchange between a resonator and its environment does not occur spontaneously. Instead, it is synthesized by engineering an interaction that exchanges pairs of photons of the cat-qubit resonator with one photon of an intentionally lossy mode referred to as the buffer⁶. The interaction Hamiltonian takes the form

$$H_i/\hbar = g_2 a^{\dagger 2} b + g_2^* a^2 b^\dagger \quad (2)$$

where b is the annihilation operator of the buffer and g_2 is the interaction strength. Adding a resonant drive on the buffer, we recover equation (1) with $\kappa_2 \approx 4|g_2|^2/\kappa_b$ and $a^2 = -\epsilon_d/g_2^*$, where ϵ_d is the drive amplitude and κ_b is the buffer energy decay rate, engineered to be larger than g_2 (refs. ^{6,27}). Conveniently, the separation $|\alpha|^2$ between the cat-qubit states is readily tunable in situ as it is proportional to the buffer drive amplitude.

We implement our cat-qubit in the circuit quantum electrodynamics (QED) architecture described in Fig. 2a, operated at 10 mK. It consists of a sputtered niobium film on a silicon substrate patterned into coplanar waveguide resonators. The cat-qubit mode resonates at $\omega_a/2\pi = 8.0381$ GHz, has a single-photon lifetime $T_1 = 3.0\ \mu\text{s}$ limited by leakage to the flux lines (see Methods) and is probed through a transmon qubit coupled to a readout resonator followed by a parametric amplifier. At the flux operating point, the buffer mode resonates at $\omega_b/2\pi = 4.8336$ GHz and has an energy decay rate of $\kappa_b/2\pi = 13$ MHz.

It is a technical challenge to engineer the interaction of equation (2) without inducing spurious effects that are detrimental for the protection of quantum information. Examples of such effects are induced relaxation^{28,29}, escape to unconfined states³⁰ and quasiparticle generation³¹. To mitigate these effects, the interaction of equation (2) is induced by a novel nonlinear dipole: the asymmetrically threaded SQUID (ATS, Fig. 2b). The ATS consists of a symmetric SQUID (superconducting quantum interference device) shunted in its centre by a large inductance, thus forming two loops. Here the inductance is built from an array of five Josephson junctions. The ATS mediates an interaction of the form $U = -2E_J \cos(\varphi_\Sigma) \cos(\varphi + \varphi_\Delta)$, where E_J is the Josephson energy of the SQUID junctions, φ is the phase across the dipole, and $2\varphi_{\Sigma,\Delta}$ are the sum and differences of flux threading the two loops (see Supplementary Information). We bias the ATS at $\varphi_\Sigma = \varphi_\Delta = \pi/2$ or, equivalently, we thread the left and right loops with flux π and 0, respectively. In addition, we drive the sum port with a radiofrequency flux pump $\epsilon(t)$. At this bias point, $U = -2E_J \sin(\epsilon(t)) \sin(\varphi)$. The ATS is coupled to the buffer and cat-qubit, so that φ is a linear combination of a , a^\dagger , b , b^\dagger and $\sin(\varphi)$ contains only odd powers of these operators. The desired interaction of equation (2) is present in the expansion of $\sin(\varphi)$, and is resonantly selected by a flux pump frequency $\omega_p = 2\omega_a - \omega_b$ (ref. ³²). In contrast with previous strategies^{6,19} (see Methods), the ATS mediates a pristine two-photon coupling, because equation (2) is the only leading order non-rotating term, the presence of the inductive shunt prevents instabilities such as the escape of the buffer to highly energetic states^{30,33}, and the device operates at a first-order flux-insensitive point (Fig. 2c). These features are key in order not to introduce inherent error processes that cannot be corrected by two-photon dissipation.

The root advantage of the cat-qubit is that its computational states $|0\rangle_a$ and $|1\rangle_a$ can be made arbitrarily long-lived simply by increasing the cat size $|\alpha|^2$, provided that $\kappa_{\text{conf}} > \kappa_{\text{err}}$. In this experiment, the dominant error is due to energy decay so

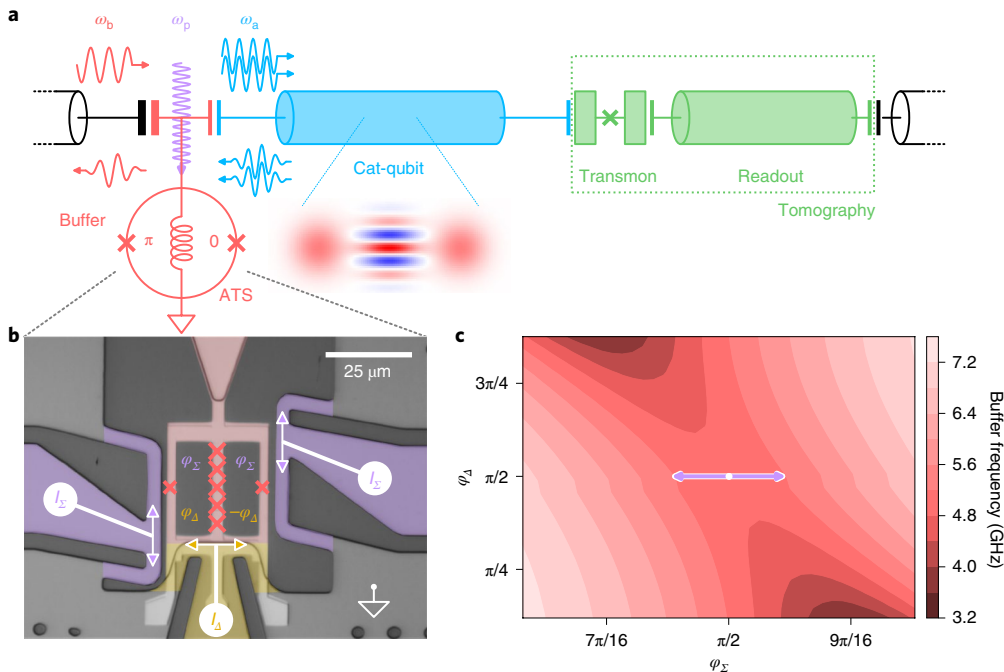


Fig. 2 | Circuit diagram and implementation. **a**, The cat-qubit resonator (blue) is coupled on one end to a transmon qubit and a readout resonator (green) to measure its Wigner function, and on the other end to the buffer (red), a lumped element resonator connected to ground through a nonlinear element coined the asymmetrically threaded SQUID (ATS). The ATS consists of a SQUID shunted by an inductance, forming two loops. Pumping the ATS at frequency $\omega_p = 2\omega_a - \omega_b$ (purple arrow), where $\omega_{a,b}$ are the cat-qubit and buffer frequencies, mediates the exchange of two photons of the cat-qubit (blue arrows) with one photon of the buffer (red arrows). **b**, False-colour optical image of the ATS. The shunt inductance is composed of an array of five Josephson junctions (marked by large red crosses). The left and right flux lines (purple) are connected to the same input through an on-chip hybrid (not represented). They carry the radiofrequency pump and the d.c. current I_Σ , which thread both loops with flux φ_Σ . The bottom flux line (yellow) carries current I_Δ and threads each loop with flux $\pm\varphi_\Delta$. Combining these two controls, we bias the ATS at the $\pi/0$ asymmetric d.c. working point. **c**, Measured buffer frequency (colour) as a function of φ_Σ (x axis) and φ_Δ (y axis), around the working point $\varphi_\Sigma, \varphi_\Delta = \pi/2, \pi/2$ (white dot). As expected, for $\varphi_\Sigma = \pi/2$ (open SQUID), the buffer frequency does not depend on φ_Δ . We operate the ATS by modulating the flux along the orthogonal direction φ_Σ (purple arrow). From this measurement, we extract all the ATS parameters (see Methods).

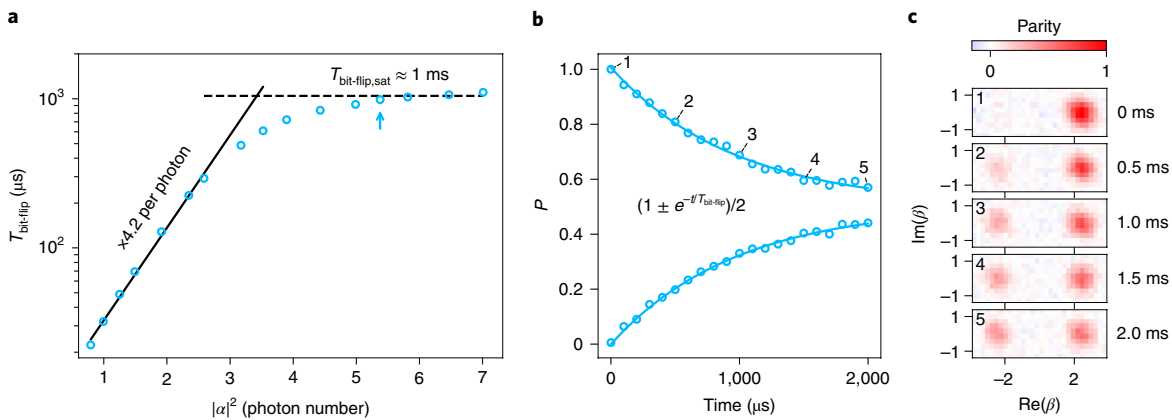


Fig. 3 | Exponential increase of the bit-flip time with cat size. **a**, The bit-flip time (y axis) is measured (open circles) as a function of the cat size defined as $|\alpha|^2$ (x axis). Up to $|\alpha|^2 \approx 3.5$, $T_{\text{bit-flip}}$ undergoes an exponential increase to ~ 0.8 ms, rising by a factor of 4.2 per added photon (the solid line results from a linear fit of the first seven data points). The bit-flip time then saturates (dashed line is a guide for the eye) for $|\alpha|^2 \geq 5$ at 1 ms, a factor of 300 larger than the cat-qubit resonator lifetime T_1 in the absence of the pump and drive. Each circle is obtained from measurements such as in **b** for the circle indicated by the blue arrow. **b**, The cat-qubit is initialized in $|0\rangle_\alpha$, for a cat size $|\alpha|^2 = 5.4$. After applying the pump and drive for a variable duration (x axis), the population P (y axis) of $|0\rangle_\alpha$ (top curve) and $|1\rangle_\alpha$ (bottom curve) is measured. The data (open circles) are fitted to decaying exponential functions (solid lines) from which we extract the bit-flip time. **c**, Each panel displays the measured normalized Wigner function of the cat-qubit after a pump and drive duration indicated on the right of each plot. Labels 1–5 mark the correspondence with **b**. The populations of $|0\rangle_\alpha$ and $|1\rangle_\alpha$ are extracted from the Wigner amplitude at $\beta = \pm\alpha$ respectively, normalized by the amplitude at $+\alpha$ at $t=0$. The cat-qubit is initialized in $|0\rangle_\alpha$ (top panel) and, over a millisecond timescale, the population escapes towards $|1\rangle_\alpha$ (lower panels). The two-photon dissipation ensures that the cat-qubit resonator state remains entirely in the steady-state manifold spanned by $|0\rangle_\alpha$ and $|1\rangle_\alpha$. Error bars smaller than the data markers' size are not represented.

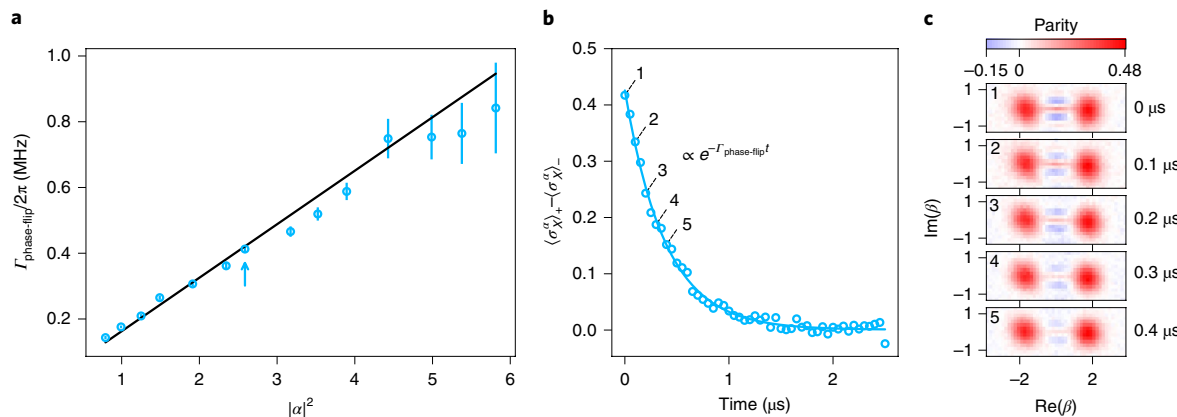


Fig. 4 | Linear increase of the phase-flip rate with the cat size. **a**, The phase-flip rate (y axis) is measured as a function of the cat size $|\alpha|^2$. The data (open circles) follow a linear trend (the solid line is a linear fit) as expected for the decay rate of a Schrödinger cat coherence $\Gamma_{\text{phase-flip}} = 2|\alpha|^2/T_{1,\text{eff}}$. We measure $T_{1,\text{eff}} = 2.0\ \mu\text{s}$ (see error budget in Methods), comparable to the intrinsic resonator lifetime of $3.0\ \mu\text{s}$. Each data point is obtained from measurements such as in **b** for the circle indicated by the blue arrow, and the error bars correspond to the uncertainty on the fitting parameter. **b**, The cat-qubit is prepared in the initial states $|\pm\rangle_\alpha$, for a cat size $|\alpha|^2 = 2.6$. After applying the pump and drive for a variable duration (x axis), $\langle \sigma_X^z \rangle_\pm$ is measured for each initial state and the difference is represented on the y axis. The X Pauli operator of the cat-qubit σ_X^α corresponds to the photon number parity. The data (open circles) are fitted to a decaying exponential (solid line) from which we extract the phase-flip rate. **c**, Each panel displays the measured normalized Wigner function of the cat-qubit after a pump and drive duration indicated on the right of each plot. Labels 1–5 mark the correspondence with **b**. The cat-qubit is initialized in the $|+\rangle_\alpha$ state and the positive and negative fringes demonstrate the quantum nature of this initial state (top panel). The fringe contrast is reduced by single photon loss, which mixes $|+\rangle_\alpha$ with $|-\rangle_\alpha$. Error bars smaller than the data markers' size are not represented.

that $\kappa_{\text{err}}/2\pi = (2\pi T_1)^{-1} = 53\ \text{kHz}$ (Extended Data Fig. 1) and $\kappa_{\text{conf}} = 2|\alpha|^2\kappa_2$ with a measured $\kappa_2/2\pi = 40\ \text{kHz}$ (from which we infer $g_2/2\pi = 360\ \text{kHz}$). Hence, we enter the regime $\kappa_{\text{conf}} > \kappa_{\text{err}}$ as soon as $|\alpha|^2 > 0.7$. We have measured that for each added photon in the cat-qubit state, the bit-flip time is multiplied by 4.2. This exponential scaling persists up to $|\alpha|^2 \approx 3.5$, and the bit-flip time saturates for $|\alpha|^2 \geq 5$ at 1 ms, a 300-fold improvement over the resonator intrinsic lifetime (Fig. 3). We expect a saturation when the corrected bit-flip rate reaches the rate of residual errors that are not correctable, such as non-local errors. In the present experiment, we attribute this saturation to the coupling with the transmon employed for the resonator tomography (see Supplementary Information), which has a thermal occupation of 1%, a lifetime $T_{1,q} = 5\ \mu\text{s}$ and is dispersively coupled to the cat-qubit resonator with a rate $\chi_{\text{qa}}/2\pi = 720\ \text{kHz}$. Over a timescale in the millisecond range, the transmon acquires a thermal excitation that shifts the cat-qubit resonator frequency by χ_{qa} . This triggers a rotation of the resonator states, which overcomes the confining potential because in this experiment $\chi_{\text{qa}} \gg \kappa_{\text{conf}}/2$ (see Methods) (note that tomography protocols compatible with smaller values of χ_{qa} have recently been demonstrated^{12,34}). During an average time $T_{1,q}$, the resonator states acquire an angle of order $\chi_{\text{qa}} T_{1,q} \gg \pi/2$. When the transmon excitation decays, the rotation stops and the two-photon dissipation brings the resonator state back into the cat-qubit computational basis. By virtue of the dissipative nature of the protection mechanism, this process may result in a bit-flip but does not cause any leakage.

Schrödinger cat states like $|\pm\rangle_\alpha$, living in a resonator with a lifetime T_1 , lose their coherence at a rate $2|\alpha|^2/T_1$ (ref. ¹). In the cat-qubit paradigm, this translates into a phase-flip rate that increases linearly with the cat size $|\alpha|^2$. In addition, our cat-qubit undergoes a flux pump, a drive and nonlinear interactions, which could further increase the phase-flip rate. We measure the phase-flip rate for increasing $|\alpha|^2$ and confirm a linear scaling (Fig. 4a). Moving towards 3D cavities and engineering ever-improving nonlinear interactions should decrease the phase-flip rate below a threshold where a line repetition code can actively correct remaining errors⁸.

In conclusion, we have observed the exponential decrease of the bit-flip rate between our cat-qubit states $|0\rangle_\alpha$ and $|1\rangle_\alpha$ as a function of their separation in phase space, while only linearly increasing their phase-flip rate. Such an exponential scaling is necessary to bridge the gap between the modest performance of quantum hardware and the exquisite performance needed for quantum computation². This was made possible by inventing a Josephson circuit that mediates a pristine nonlinear coupling between our cat-qubit mode and its environment. Further improving the lifetime of the cavity to the state of the art of a millisecond³⁵ and a cat size of $|\alpha|^2 \approx 5$ (resp. 10) should lead to a bit-flip time of $\sim 1\ \text{s}$ (resp. $0.5\ \text{h}$), and a phase-flip time of $\sim 100\ \mu\text{s}$ (resp. $50\ \mu\text{s}$). Because the bit-flip time is much longer than the phase-flip time, the cat-qubit is said to have biased noise. Building surface codes out of biased noise qubits could considerably increase the error correcting threshold²⁰. Another strategy leverages a unique feature of the cat-qubit: its 2D phase space. Excursions in this phase space form a universal set of gates without using magic states, and phase-flips are corrected in a linear repetition code architecture⁸. These proposals are promising routes towards significantly reducing the hardware overhead for QEC.

Online content

Any methods, additional references, Nature Research reporting summaries, source data, extended data, supplementary information, acknowledgements, peer review information; details of author contributions and competing interests; and statements of data and code availability are available at <https://doi.org/10.1038/s41567-020-0824-x>.

Received: 24 September 2019; Accepted: 4 February 2020;
Published online: 16 March 2020

References

1. Haroche, S. & Raimond, J.-M. *Exploring the Quantum* (Oxford Univ. Press, 2006).
2. Fowler, A. G., Mariantoni, M., Martinis, J. M. & Cleland, A. N. Surface codes: towards practical large-scale quantum computation. *Phys. Rev. A* **86**, 032324 (2012).

3. Kitaev, A. Y. Unpaired majorana fermions in quantum wires. *Phys. Uspekhi* **44**, 131–136 (2001).
4. Mourik, V. et al. Signatures of Majorana fermions in hybrid superconductor–semiconductor nanowire devices. *Science* **336**, 1003–1007 (2012).
5. Wolinsky, M. & Carmichael, H. J. Quantum noise in the parametric oscillator: from squeezed states to coherent-state superpositions. *Phys. Rev. Lett.* **60**, 1836–1839 (1988).
6. Leghtas, Z. et al. Confining the state of light to a quantum manifold by engineered two-photon loss. *Science* **347**, 853–857 (2015).
7. Mirrahimi, M. et al. Dynamically protected cat-qubits: a new paradigm for universal quantum computation. *New J. Phys.* **16**, 045014 (2014).
8. Guillaud, J. & Mirrahimi, M. Repetition cat qubits for fault-tolerant quantum computation. *Phys. Rev. X* **9**, 041053 (2019).
9. Shor, P. Scheme for reducing decoherence in quantum memory. *Phys. Rev. A* **52**, 2493–2496 (1995).
10. Steane, A. M. Error correcting codes in quantum theory. *Phys. Rev. Lett.* **77**, 793–797 (1996).
11. Flühmann, C. et al. Encoding a qubit in a trapped-ion mechanical oscillator. *Nature* **566**, 513–517 (2019).
12. Campagne-Ibarcq, P. et al. A stabilized logical quantum bit encoded in grid states of a superconducting cavity. Preprint at <https://arxiv.org/pdf/1907.12487.pdf> (2019).
13. Brooks, P., Kitaev, A. & Preskill, J. Protected gates for superconducting qubits. *Phys. Rev. A* **87**, 052306 (2013).
14. Albrecht, S. M. et al. Exponential protection of zero modes in Majorana islands. *Nature* **531**, 206–209 (2016).
15. Lin, Y.-H. et al. Demonstration of protection of a superconducting qubit from energy decay. *Phys. Rev. Lett.* **120**, 150503 (2018).
16. Earnest, N. et al. Realization of a Λ system with metastable states of a capacitively shunted fluxonium. *Phys. Rev. Lett.* **120**, 150504 (2018).
17. Smith, W. C., Kou, A., Xiao, X., Vool, U. & Devoret, M. H. Superconducting circuit protected by two-Cooper-pair tunneling. *npj Quantum Inf.* **6**, 8 (2020).
18. Puri, S., Boutin, S. & Blais, A. Engineering the quantum states of light in a Kerr-nonlinear resonator by two-photon driving. *npj Quantum Inf.* **3**, 18 (2017).
19. Touzard, S. et al. Coherent oscillations inside a quantum manifold stabilized by dissipation. *Phys. Rev. X* **8**, 021005 (2018).
20. Tuckett, D. K., Bartlett, S. D. & Flammia, S. T. Ultrahigh error threshold for surface codes with biased noise. *Phys. Rev. Lett.* **120**, 050505 (2018).
21. Tuckett, D. K. et al. Tailoring surface codes for highly biased noise. *Phys. Rev. X* **9**, 041031 (2019).
22. Tuckett, D. K., Bartlett, S. D., Flammia, S. T. & Brown, B. J. Fault-tolerant thresholds for the surface code in excess of 5% under biased noise. Preprint at <https://arxiv.org/pdf/1907.02554.pdf> (2019).
23. Grimm, A. et al. The Kerr-cat qubit: stabilization, readout and gates. Preprint at <https://arxiv.org/pdf/1907.12131.pdf> (2019).
24. Puri, S. et al. Bias-preserving gates with stabilized cat qubits. Preprint at <https://arxiv.org/pdf/1905.00450.pdf> (2019).
25. Leghtas, Z. et al. Hardware-efficient autonomous quantum memory protection. *Phys. Rev. Lett.* **111**, 120501 (2013).
26. Gottesman, D., Kitaev, A. & Preskill, J. Encoding a qubit in an oscillator. *Phys. Rev. A* **64**, 012310 (2001).
27. Carmichael, H. J. *Statistical Methods in Quantum Optics 2* (Springer, 2008).
28. Sank, D. et al. Measurement-induced state transitions in a superconducting qubit: beyond the rotating wave approximation. *Phys. Rev. Lett.* **117**, 190503 (2016).
29. Gao, Y. Y. et al. Programmable interference between two microwave quantum memories. *Phys. Rev. X* **8**, 021073 (2018).
30. Lescanne, R. et al. Escape of a driven quantum Josephson circuit into unconfined states. *Phys. Rev. Appl.* **11**, 014030 (2019).
31. Wang, C. et al. Measurement and control of quasiparticle dynamics in a superconducting qubit. *Nat. Commun.* **5**, 5836 (2014).
32. Vrajitoarea, A., Huang, Z., Groszkowski, P., Koch, J. & Houck, A. A. Quantum control of an oscillator using a stimulated Josephson nonlinearity. *Nat. Phys.* **16**, 211–217 (2019).
33. Verney, L., Lescanne, R., Devoret, M. H., Leghtas, Z. & Mirrahimi, M. Structural instability of driven Josephson circuits prevented by an inductive shunt. *Phys. Rev. Appl.* **11**, 024003 (2019).
34. Touzard, S. et al. Gated conditional displacement readout of superconducting qubits. *Phys. Rev. Lett.* **122**, 080502 (2019).
35. Reagor, M. et al. Quantum memory with millisecond coherence in circuit QED. *Phys. Rev. B* **94**, 014506 (2016).

Publisher's note Springer Nature remains neutral with regard to jurisdictional claims in published maps and institutional affiliations.

© The Author(s), under exclusive licence to Springer Nature Limited 2020

Methods

Device fabrication and wiring. The circuit was fabricated on a 280 μm -thick wafer of intrinsic silicon (resistivity $>10,000 \Omega\text{ cm}$). The silicon wafer was dipped in a 1:7 buffered solution of hydrofluoric acid (HF) for 2 min (ref. ³⁶), rinsed in deionized (DI) water and immediately loaded in a sputtering system. After one night of pumping, we sputtered 120 nm of Nb onto the chip. Optical resist (S1805) was spun on and large features ($>1 \mu\text{m}$) were patterned with a laser writer. After development (MF319), the sample was etched in SF₆ with a 20 s overetch, followed by liftoff (acetone at 50 °C). We then spun a bilayer of methacrylic acid/methyl methacrylate (EL11) and poly(methyl methacrylate) (A6). The Josephson junctions were patterned by electron-beam lithography. A single Dolan bridge was used to make the small junctions of the ATS and of the transmon, and a series of three Dolan bridges were used to delimit the five-junction array, which served as the ATS inductor. The development took place in a 3:1 isopropyl alcohol (IPA)/water solution at 6 °C for 90 s, followed by 10 s in IPA. The chip was then loaded into an electron-beam evaporator. We started with a thorough argon ion milling for 2 min with the sample at an angle of $\pm 30^\circ$, which served to clean the substrate and contact the Nb. We then evaporated 35 nm and 70 nm of aluminium, at $\pm 30^\circ$ angles, separated by an oxidation step of 200 mbar of pure oxygen for 10 min. The full device layout and wiring are presented in Extended Data Figs. 3 and 4.

Circuit parameters. Most of the circuit parameters can be readily deduced from standard circuit QED measurements and are presented in Extended Data Fig. 1. Here we explain the methodology we used to deduce the six dipole parameters of Extended Data Fig. 8 (Extended Data Fig. 2) and the mapping of (I_Σ, I_d) to $(\varphi_\Sigma, \varphi_d)$. Independently of this mapping, the ATS saddle point is unambiguously found. At this flux point, $E_j \cos(\varphi_\Sigma) = 0$, and we directly measure $\omega_{a,0}$ and $\omega_{b,0}$. The Josephson energy E_j and the inductive energy $E_{l,b}$ (formed by an array of five Josephson junctions) are computed from the Ambegaokar–Baratoff formula using the room-temperature measurements of neighbouring test junction resistances. The general linear transformation mapping (I_Σ, I_d) to $(\varphi_\Sigma, \varphi_d)$ is found by fitting by the measured buffer frequency as a function of (I_Σ, I_d) (Extended Data Fig. 5c,d). The impedance Z_a of the cat-qubit resonator is estimated from the aspect ratio of the coplanar waveguide geometry. The charging energy $E_{c,c}$ of the coupling capacitor is adjusted to match the measured anticrossing of the buffer and cat-qubit mode when I_Σ is varied (Extended Data Fig. 5b).

Cat-qubit error budget. The bit-flip time is limited by the dispersive coupling of the cat-qubit to the transmon (see main text). The phase-flip time can be expressed as $T_{1,\text{eff}}/2|\alpha|^2$, where $T_{1,\text{eff}} = 2 \mu\text{s}$ is limited by the resonator T_1 and parasitic effects due to the strong pump. The resonator T_1 is limited by leakage to the flux lines (which do not contain Purcell filters). The parasitic effects have several origins. First, the pump does not address exclusively the common flux (φ_Σ) , thus populating the buffer mode, which usually introduces losses³⁷. Moreover, the inductive shunt is not an ideal inductor, but is instead composed of a chain of five Josephson junctions. These junctions can undergo phase slips³⁸, and their high yet bounded potential does not prevent them from escaping to high energy states³⁹. Finally, the asymmetry of the SQUID junctions induces undesirable interactions. All these effects contribute to reducing the T_1 in the presence of the pump. In the future, we plan to improve the ATS element (symmetry, inductive shunt) and improve the filtering and thermalization of the pump lines.

Tuning the cat-qubit. As explained in the main text, the flux point at which the ATS should operate is a saddle point of the buffer frequency map. It is very simple to find experimentally, as we do not need to know the full mapping between (I_Σ, I_d) and $(\varphi_\Sigma, \varphi_d)$ to recognize a saddle point. There are actually two types of saddle points, as one can see in Extended Data Fig. 5: those that are tilted to the left and those that are tilted to the right. If the two junctions forming the SQUID of the ATS were perfectly symmetric, these points would be equivalent. Otherwise, the buffer acquires a Kerr nonlinearity and the two points differ by the sign of this Kerr. We chose a positive Kerr point so that, from the point of view of the cat-qubit resonator, the positive Kerr induced by the buffer and the negative Kerr induced by the transmon tend to compensate. Once we find the buffer and cat-qubit frequencies, we perform two-tone spectroscopy on the buffer (Extended Data Fig. 6). A weak tone, referred to as the drive, probes the buffer resonance and the pump is swept in the relevant frequency range (around $2\omega_a - \omega_b$). When the two-to-one exchange occurs between the buffer and the cat-qubit, we observe a sharp feature within the buffer resonance (Extended Data Fig. 6a,b). The width of this feature depends on the weak tone strength and, more importantly, on the pump power. The pump power is pushed until before this feature becomes ill-defined, when other nonlinear dynamics start to play a significant role. On the cat-qubit side, within this feature, the drive combined with the pump populates the cat-qubit resonator. We check this by measuring the parity of the cat-qubit resonator and verify that it decays after a timescale T_1 (Extended Data Fig. 6c). We tune the pump and buffer frequencies in the middle of the decayed area. The width along Δ of this region enables us to determine κ_2 . We perform the cat-qubit resonator full tomography after a long ($20\mu\text{s} \gg \kappa_a^{-1}$) pump and drive pulse (Extended Data Fig. 7a) and we set the drive amplitude to produce the desired cat size (Extended Data

Fig. 7b). The cat-qubit characteristics ($T_{\text{bit-flip}}, \Gamma_{\text{phase-flip}}$, time evolution of the Wigner function) measurements are described in the main text.

Comparison to other implementations. In previous experiments^{40,41}, a single Josephson junction mediated the two-photon interaction, which is therefore tied to the dispersive coupling by $g_2 = \chi_{ba}\xi_p/2$, where ξ_p is the pump amplitude. Increasing g_2 (and hence $\kappa_2 = 4g_2^2/\kappa_b$) requires increasing the pump amplitude ξ_p , which causes dissipation⁴² and instabilities^{39,43}. In this Letter, the ATS was invented to mediate a two-photon interaction without mediating a dispersive interaction between the buffer and cat-qubit. In the following we explain why this dispersive coupling, combined with a finite thermal occupancy of the buffer, can spoil the suppression of bit flips. To induce the desired two-photon interaction, the pump and drive frequencies ω_p and ω_d are tuned to satisfy the following frequency matching condition $\Delta \equiv \omega_a - (\omega_d + \omega_p)/2 = 0$, where we fix $\omega_d = \omega_b$. When a thermal photon enters the buffer, it detunes the cat qubit frequency and consequently shifts Δ by the dispersive coupling χ_{ba} . However, the linewidth of this matching condition is of the order of $\kappa_a\alpha^2$ (see Extended Data Fig. 6d and equation (27) of the Supplementary Information), and therefore the two-photon interaction will be deactivated unless the condition $\kappa_2\alpha^2 \gg \chi_{ba}$ is satisfied (condition (1)). Fulfilling condition (1) is sufficient, but not necessary, for thermal photons in the buffer not to cause bit flips. Assuming the thermal photon deactivates the pumping process, while this photon subsides in the buffer, the cat qubit rotates in phase space at an angular frequency χ_{ba} . The thermal photon will eventually decay after a random time of the order of the buffer lifetime $1/\kappa_b$, leaving the cat-qubit state with a random angle in phase space of order χ_{ba}/κ_b . The two-photon stabilization is reestablished and attracts the rotated cat-qubit state to its closest attractor. If this angle satisfies the condition $\chi_{ba}/\kappa_b \ll \pi/2$ (condition (2)), the initial cat-qubit state is restored, otherwise a bit flip occurs at a rate of order $n_{th,b}\kappa_b$ where $n_{th,b}$ is the buffer thermal occupancy. We will now show that previous implementations met neither condition (1) nor condition (2). In this experiment we do not meet condition (1), but we meet condition (2). In ref. ⁴⁰, this leads, to $\kappa_2\alpha^2/\chi_{ba} \approx 1$, and hence condition (1) is barely met even for the largest measured α^2 . However $\chi_{ba}/\kappa_b = 0.9$, hence condition (2) is not met. In ref. ⁴¹, the buffer to cat-qubit interaction was mediated through a transmon, which was the bottleneck of the experiment. We find $\kappa_2\alpha^2/\chi_{ba} \approx 0.01$, and hence condition (1) is not met. Moreover $\chi_{ba}/\kappa_b = 231$ and condition (2) is not met. In this paper, We obtain $\kappa_2\alpha^2/\chi_{ba} \approx 0.25$, and hence condition (1) is not met. However $\chi_{ba}/\kappa_b = 0.06$, hence condition (2) is met. An ideal ATS element with identical small junctions and a perfect flux biasing would have a zero χ_{ba} . In this experiment, χ_{ba} was made small enough for thermal photons in the buffer not to induce bit-flips.

Data availability

The data that support the plots within this paper and other findings of this study are available from the corresponding author upon reasonable request.

References

36. Bruno, A. et al. Reducing intrinsic loss in superconducting resonators by surface treatment and deep etching of silicon substrates. *Appl. Phys. Lett.* **106**, 182601 (2015).
37. Sank, D. et al. Measurement-induced state transitions in a superconducting qubit: beyond the rotating wave approximation. *Phys. Rev. Lett.* **117**, 190503 (2016).
38. Pop, I. M. et al. Measurement of the effect of quantum phase slips in a Josephson junction chain. *Nat. Phys.* **6**, 589–592 (2010).
39. Lescanne, R. et al. Escape of a driven quantum Josephson circuit into unconfined states. *Phys. Rev. Appl.* **11**, 014030 (2019).
40. Touzard, S. et al. Coherent oscillations inside a quantum manifold stabilized by dissipation. *Phys. Rev. X* **8**, 021005 (2018).
41. Leghtas, Z. et al. Confining the state of light to a quantum manifold by engineered two-photon loss. *Science* **347**, 853–857 (2015).
42. Gao, Y. Y. et al. Programmable interference between two microwave quantum memories. *Phys. Rev. X* **8**, 021073 (2018).
43. Verney, L., Lescanne, R., Devoret, M. H., Leghtas, Z. & Mirrahimi, M. Structural instability of driven Josephson circuits prevented by an inductive shunt. *Phys. Rev. Appl.* **11**, 024003 (2019).
44. Reed, M. D. et al. Fast reset and suppressing spontaneous emission of a superconducting qubit. *Appl. Phys. Lett.* **96**, 203110 (2010).
45. Frattini, N. E., Sivak, V. V., Lingenfelter, A., Shankar, S. & Devoret, M. H. Optimizing the nonlinearity and dissipation of a snail parametric amplifier for dynamic range. *Phys. Rev. Appl.* **10**, 054020 (2018).

Acknowledgements

We acknowledge fruitful discussions with P. Rouchon and C. Smith. Z.L. acknowledges support from ANR project ENDURANCE and EMERGENCES grant ENDURANCE of Ville de Paris. A.S. acknowledges support from ANR project HAMROQS. The devices were fabricated within the consortium Salle Blanche Paris Centre. This work has been supported by the Paris Île-de-France Region in the framework of DIM SIRTEQ. M.M. acknowledges support from ARO under grant no. W911NF-18-1-0212. Z.L. acknowledges Mines-ParisTech as his primary affiliation.

Author contributions

R.L. designed, fabricated and measured the device, and analysed the data. R.L. and Z.L. conceived the ATS element with help from B.H. and T.P. R.L. and Z.L. wrote the paper with input from all authors. M.V. fabricated the parametric amplifier. T.K. and M.D. provided experimental support. A.S. and M.M. provided theory support. Z.L. managed the project. All authors contributed to extensive discussions of the results.

Competing interests

The authors declare no competing interests.

Additional information

Extended data is available for this paper at <https://doi.org/10.1038/s41567-020-0824-x>.

Supplementary information is available for this paper at <https://doi.org/10.1038/s41567-020-0824-x>.

Correspondence and requests for materials should be addressed to Z.L.

Peer review information *Nature Physics* thanks Christopher Eichler and the other, anonymous, reviewer(s) for their contribution to the peer review of this work.

Reprints and permissions information is available at www.nature.com/reprints.

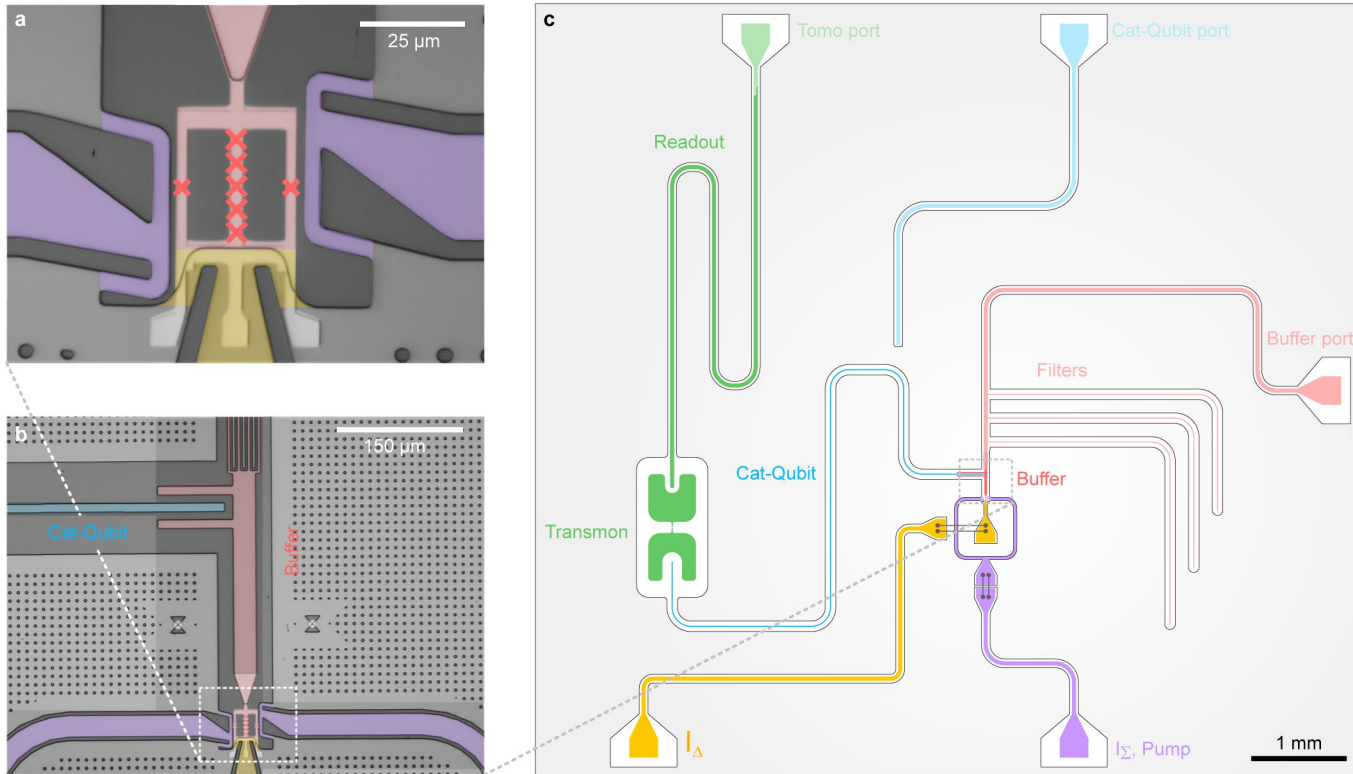
Cat-qubit mode		Buffer		Transmon	
$\omega_a/2\pi$	8.03805 GHz	$\omega_b/2\pi$	4.8336 GHz	$\omega_q/2\pi$	4.4156 GHz
$\omega_{a,0}/2\pi$	8.0389 GHz	$\omega_{b,0}/2\pi$	4.886 GHz	$T_{1,q}$	5 μ s
T_1	3 μ s	$\kappa_b/2\pi$	13 MHz	$T_{2,q}$	8 μ s
$\kappa_a/2\pi$	53 kHz	$\chi_{bb}/2\pi$	-32 MHz	$\chi_{qq}/2\pi$	180 MHz
$\chi_{aa}/2\pi$	-7 kHz	$\chi_{ba}/2\pi$	0.79 MHz	$\chi_{qa}/2\pi$	720 kHz
				π/χ_{qa}	0.69 μ s

Pump		Readout	
$\omega_p/2\pi$	11.2425 GHz	$\omega_r/2\pi$	6.4598 GHz
		$\kappa_r/2\pi$	1.47 MHz

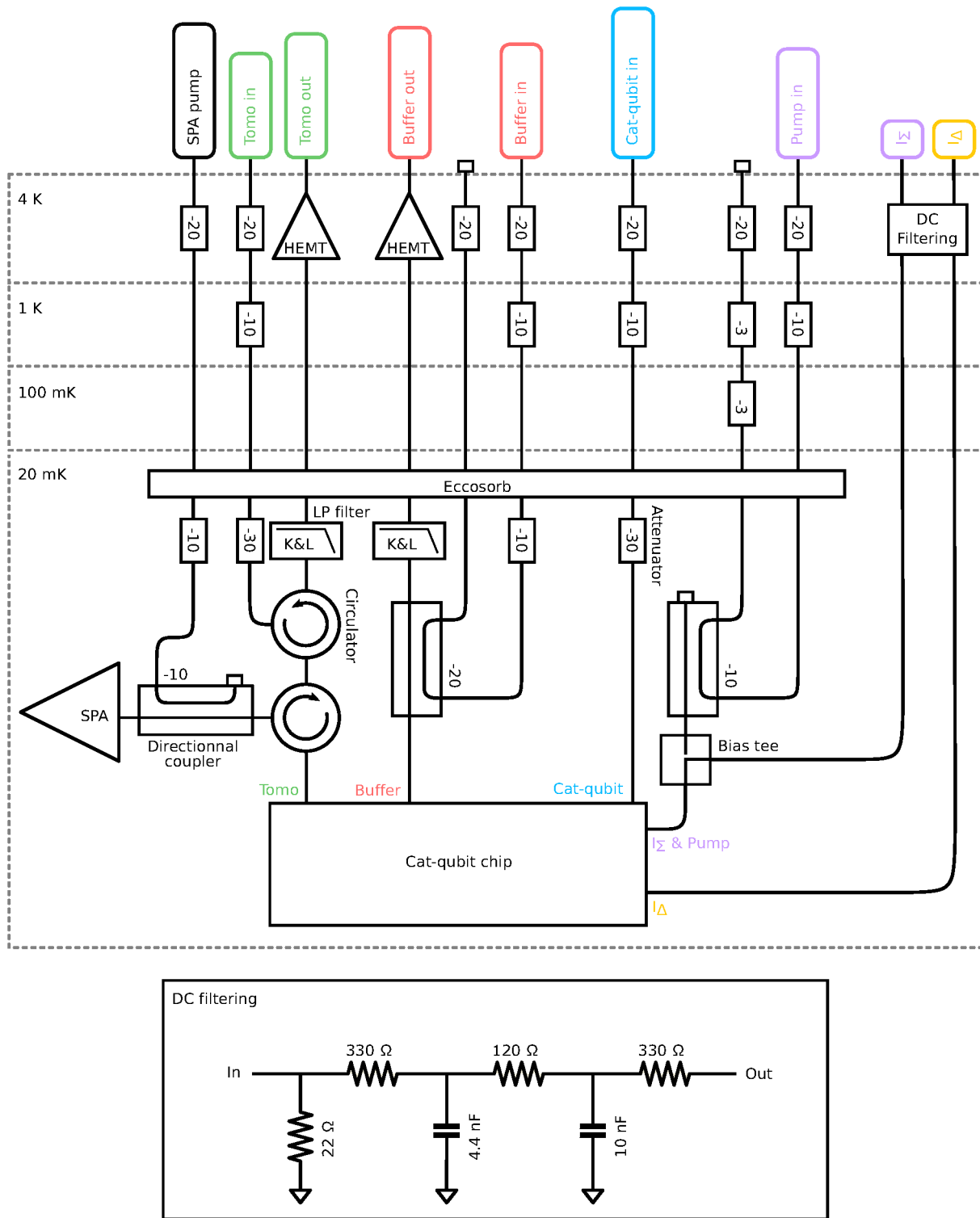
Extended Data Fig. 1 | Measured system parameters at the ATS working point. The pump shifts the cat-qubit resonator and buffer frequencies. The frequencies in the absence of the pump are noted $\omega_{a/b,0}$ and those in its presence are denoted $\omega_{a/b}$. The Kerr couplings χ_{mn} enter the full Hamiltonian in the form $-\chi_{mn}m^\dagger mn^\dagger n$ when $m \neq n$ and $-\frac{\chi_{mm}}{2}m^\dagger m^2$, where m, n denote the mode indices.

Circuit parameters		Dipole parameters	
$\omega_{a,0}/2\pi$	8.0389 GHz	$E_{L,a}/h$	96.6 GHz
Z_a	90 Ω	$E_{C,a}/h$	92.7 MHz
$\omega_{b,0}/2\pi$	4.886 GHz	$E_{C,b}/h$	73.5 MHz
$E_{C,c}/h$	720 MHz	$E_{C,c}/h$	720 MHz
$E_{L,b}/h$	45 GHz	$E_{L,b}/h$	45 GHz
E_J/h	90 GHz	E_J/h	90 GHz

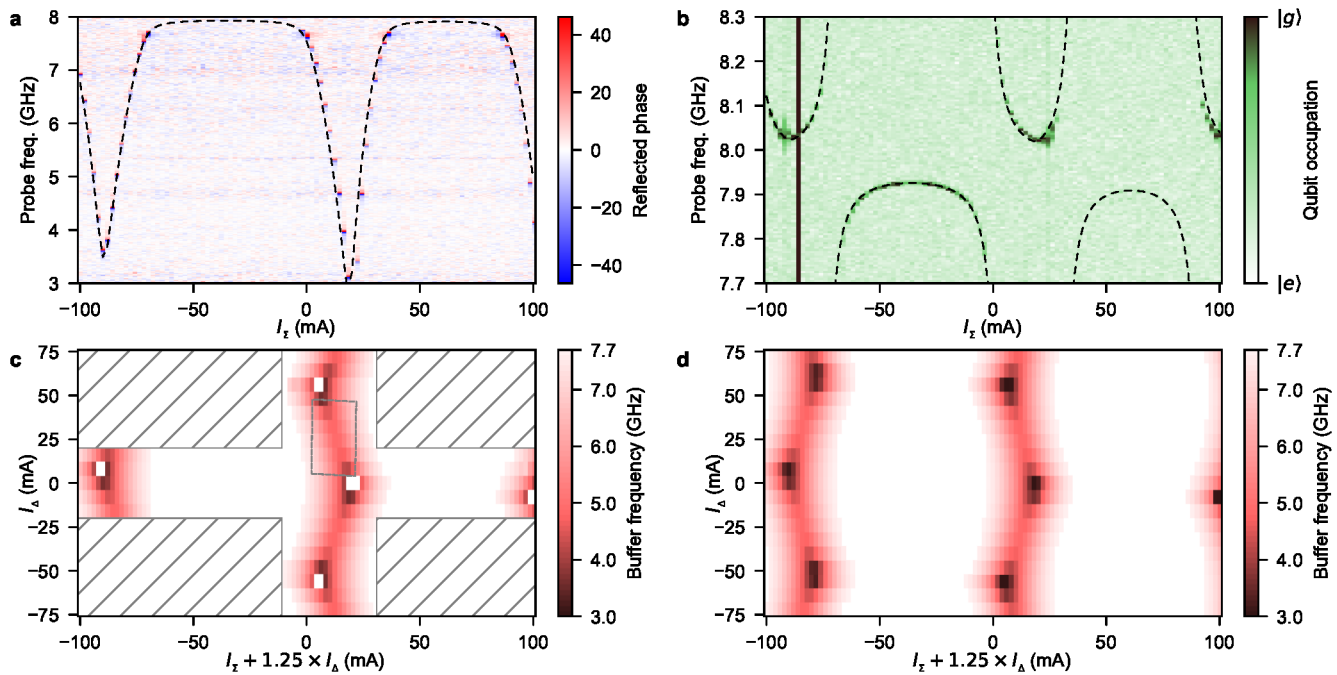
Extended Data Fig. 2 | Underlying parameters of the cat-qubit and buffer resonators. Measured and estimated circuit parameters (left), and their corresponding dipole energies (right).



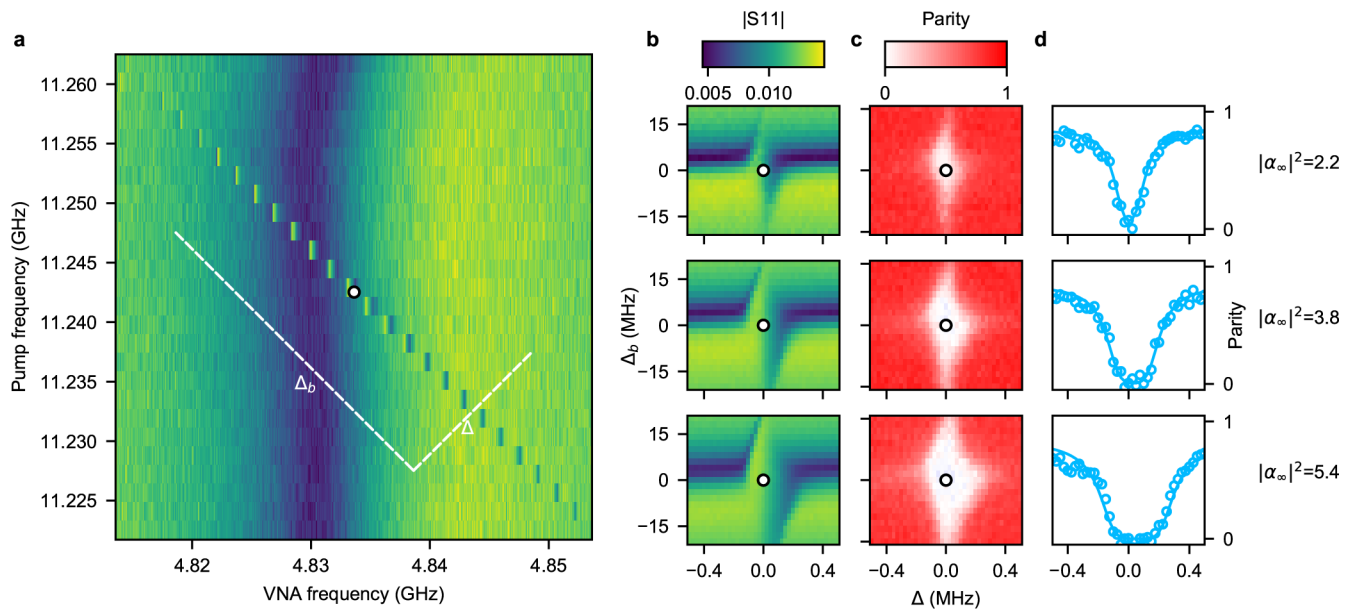
Extended Data Fig. 3 | Full device layout. **a**, False color optical image of the ATS. Note that the 5 junction symbols are separated for clarity, the actual junctions are much closer and centered in the middle of the arm. **b**, False color optical image of the buffer. The buffer (red) is strongly coupled to its transmission line via an interdigitated capacitor (top). It is also capacitively coupled to the cat-qubit resonator (blue). This is actually a picture of a twin sample where this coupling was smaller. In panel **c**, the real size of the coupling capacitor is shown. **(c)** Full device layout. The cat-qubit resonator is coupled on its other side to a transmon qubit, itself coupled to a readout resonator which together enable to perform the cat-qubit tomography. After the interdigitated capacitor, the buffer input is filtered via three $\lambda/4$ -stub filters. These stop-band filters are centered at the cat-qubit resonance frequency to mitigate its direct coupling to the input line of the buffer⁴⁴ (**b**). The on-chip hybrid along the pump path (purple), equally splits the pump tone to RF-flux bias the ATS with the right symmetry. The black lines linking two dots are a schematic representation of the crucial wirebonds of the device. The wirebonds linking the pump input to the on-chip hybrid were implemented to reduce the area of the loop delimited by the center conductor and the ground plane, leading to a reduced sensitivity to flux noise.



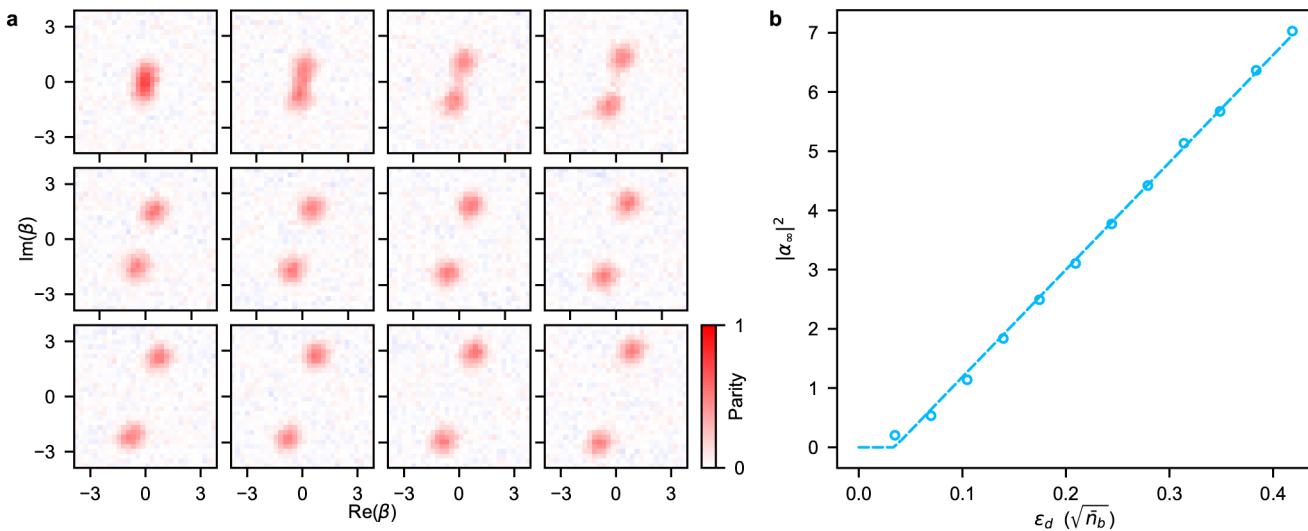
Extended Data Fig. 4 | RF and DC wiring of the dilution refrigerator. Note that the pump and drive tones are attenuated at the base plate via directional couplers so that the attenuated power is dissipated at higher fridge stages, far from the sample. The I_x DC current and the RF pump signal are combined at 20 mK with a bias-tee. We have used a homemade ‘Snail Parametric Amplifier’ (SPA)⁴⁵.



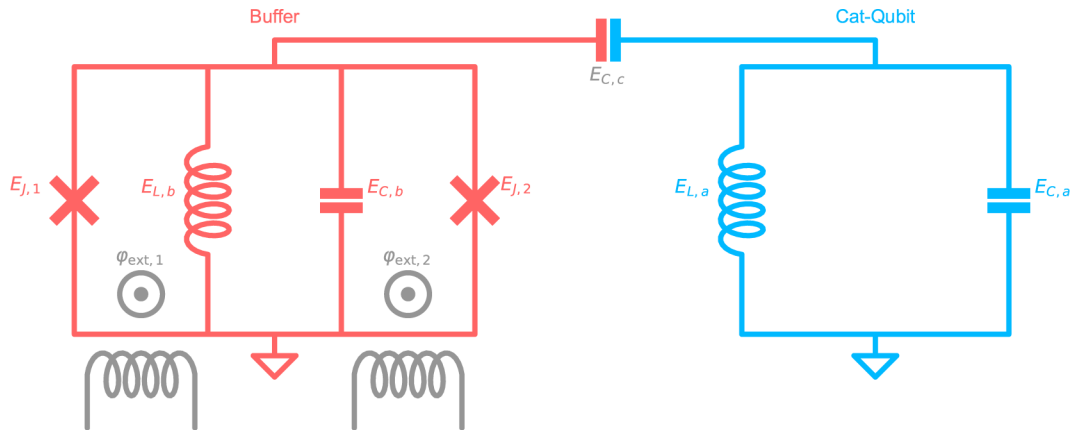
Extended Data Fig. 5 | Flux dependence. **a**, Buffer spectroscopy. Phase of the reflected probe signal (colormap) on the buffer port as a function of I_z (x-axis) and probe frequency (y-axis). The buffer frequency follows an arch-like pattern typical of SQUID-based devices. The probing frequency range is limited to 3–8 GHz due to the 4–8 GHz circulator on the output line. The black dashed line represents the expected buffer/cat-qubit frequency for the best fitting parameter set. The slight aperiodicity may be explained by small asymmetries in the loop areas of the ATS. **b**, Cat-qubit resonator two-tone spectroscopy. A continuous probe is applied on the cat-qubit resonator at various frequencies (y-axis) and a second tone attempts to π -pulse the qubit on resonance. When the probe populates the cat-qubit, the qubit shifts in frequency due to the cross-Kerr coupling, and is insensitive to the π -pulse. The resulting qubit occupation is plotted in color and we repeat the experiment for various values of I_z (x-axis). The black dashed line represents the expected buffer/cat-qubit frequency for the best fitting parameter set. The black vertical line corresponds to a flux bias where the buffer is at the qubit frequency resulting in a strong decrease in the qubit lifetime. **c**, For each value of I_z (x-axis) and I_A (y-axis), we extract the buffer frequency from a spectroscopy measurement (panel **a**) and report it in color (white is when the resonance frequency is beyond the measurement range). Contrary to what they were designed for, the two flux lines do not perfectly apply symmetric (I_z) and antisymmetric (I_A) bias on the ATS. We compensate for this imbalance while taking the data by shifting the I_z span for each value of I_A as indicated on the x-axis label. Data were only taken on the area outside the hatched regions to prevent the heating of the dilution refrigerator beyond a tolerable temperature. The grey dashed-rectangle corresponds to the flux range presented in Fig. 2 of the main text. **d**, Simulated flux dependence of the buffer mode for the best fitting parameter set.



Extended Data Fig. 6 | Tuning the pump and drive frequencies. **a**, Reflected relative drive amplitude (VNA measurement) as a function of drive frequency (x-axis) and pump frequency (y-axis). When $\omega_p = 2\omega_a - \omega_d$, a sharp feature indicates that the two-to-one photon exchange is resonant and as expected, it has a slope -1 . To observe this feature, we switch to the basis $\Delta = (\Delta_{\text{pump}} + \Delta_{\text{drive}})/2$, $\Delta_b = (\Delta_{\text{pump}} - \Delta_{\text{drive}})/2$, the orientation of which is given by the white dashed lines. **b,c**, Reflected relative drive amplitude (color) and parity of the cat-qubit resonator (red) as a function of Δ (x-axis) and Δ_b (y-axis) for increasing drive amplitude (top to bottom). The drive amplitude is expressed in units of the cat size $|\alpha_\infty|^2$ which is calibrated using the data of Extended Data Fig. 7. **c**, When the two-to-one photon exchange is resonant, the cat-qubit resonator is displaced and the parity drops to 0 if we measure after a time greater than κ_a^{-1} . We also perform the cat-qubit resonator tomography and verify that the resonator is in a balanced mixture of $|0\rangle_a$ and $|1\rangle_a$. In all these plots, the white circles correspond to the chosen pump and drive frequencies. We verify that for all used drive amplitudes, this point remains centered in the resonant range. Therefore, we do not need to adapt the drive and pump frequencies when increasing the cat size. **d**, Cut of the color plot (**c**) at $\Delta_b = 0$ representing the parity (open circle) of the cat-qubit steady state as a function of Δ . The relation of Eq. (26) of the supplementary information shows that the frequency window over which a non-trivial state is stabilized in the cavity scales as $2\kappa_2|\alpha|^2$. This enables us to determine κ_2 assuming photon loss is the main loss mechanism. We fit (solid line) the measured parity with the expected steady-state parity (QuTiP) where the two fitting parameters are the parity contrast and κ_2 . We find $\kappa_2/2\pi = 40$ kHz.



Extended Data Fig. 7 | Increasing the cat-qubit size. **a**, Measured Wigner distribution of the cat-qubit state as a function of drive amplitude (left to right, top to bottom) after a pump and drive pulse duration of $20\mu\text{s}$. **b**, Fitted cat size $|\alpha_\infty|^2$ (open circles) as a function of the drive amplitude ϵ_d . The drive amplitude is expressed in terms of the square root of the photon number the buffer would contain without the conversion process. For each Wigner distribution of panel **(a)**, we fit a sum of two 2D-Gaussian functions (coherent states) diametrically opposed which are separated by a distance $2|\alpha_\infty|$. Note that for simplicity, in the main text, we use $|\alpha|^2$ instead of $|\alpha_\infty|^2$. In the presence of single photon loss at rate κ_o , we expect $|\alpha_\infty|^2$ to follow the relation of Eq. (20) of the supplementary information (dashed line): a linear dependence on ϵ_d when $|\alpha|^2 > \kappa_o/(2\kappa_2)$. By fitting this relation to the data, we calibrate the x-axis scaling.



Extended Data Fig. 8 | Equivalent circuit diagram. The cat-qubit resonator (blue) is represented by a linear LC resonator with charging energy $E_{C,a}$ and inductive energy $E_{L,a}$. It is capacitively coupled through a capacitor of charging energy $E_{C,c}$ to the buffer (red) which consists of a capacitively shunted ATS element. The ATS, introduced in the main text, is formed by two Josephson junctions (crosses) of Josephson energies $E_{J,1}$ and $E_{J,2}$ split by an inductor of inductive energy $E_{L,b}$. In practice, this inductor is made out of 5 large Josephson junctions. Flux lines represented as grey inductors thread magnetic flux through the two ATS loops. One recovers the circuit of Fig. 2 by setting $\varphi_{ext,1} = \pi$ and $\varphi_{ext,2} = 0$. Not shown here: the buffer is capacitively coupled to a transmission line and the cat-qubit resonator is coupled to a transmon qubit, its readout resonator and a transmission line.